Closed-form solution of fundamental frequency of steel-concrete hybrid wind turbine tower

Shou-Zhen Li[a,b], Xu-Hong Zhou[a,b], Yu-Hang Wang[a,b,*], Dan Gan[a,b], Xiao-Wei Deng[c]

[a] School of Civil Engineering, Chongqing University, Chongqing 400000, China

[b] Key Laboratory of New Technology for Construction of Cities in Mountain Area, Chongqing 400045, China

[c] The University of Hong Kong, Pokfulam, Hong Kong 999077, China

Abstract

With the development of wind power energy, the steel-concrete hybrid tower has been gradually popularized as the onshore tall wind turbine tower. To avoid the resonant response that brings violent damage to the wind turbine tower, the fundamental frequency of the hybrid tower must be carefully analyzed. This study develops a closed-form solution of the fundamental frequency of the hybrid tower, where the abrupt changes of cross-section and material properties, the effect of prestressing, and the mass and rotary inertia of the wind turbine are taken into account. It provides an effective way to obtain the fundamental frequency in the preliminary design of the hybrid tower. The effectiveness of the proposed solution is validated by comparing it with the results of finite element analysis, showing good agreement. By using the proposed solution, a parametric analysis is conducted to investigate the variation rules of the fundamental frequency to the design parameters. It indicates that with the variation of the proportion of the concrete/steel segments, the correlations between the fundamental frequency and the design parameters also change significantly. The parametric analysis conducted

herein may provide instructive guidelines to adjust the parameters in the preliminary design of the hybrid tower.

Keywords: Steel-concrete hybrid structure, Onshore wind turbine tower, Closed-form solution, Fundamental frequency, Parametric analysis.

1. Introduction

With the depletion of fossil energy and the aggravation of environmental pollution, the world is devoted to the research and promotion of clean energy. Wind power energy, which is highly efficient and renewable, plays an important role in promoting the construction of a low-carbon and environment-friendly society [1-4]. With the development of the wind power industry, the locations of the wind farm are converting from high-wind-speed areas to low-wind-speed areas [5,6]. To obtain a more stable wind speed and improve the generation efficiency of wind power in the low-wind-speed area, strategies aimed at increasing hub heights have been proposed, which means that the wind turbine tower has to be built with a taller height [7,8]. This puts forward higher requirements for the load-bearing capacity of the support structure to ensure the normal operation of the upper wind turbine.

The tubular steel tower, which is the most common support structure, has many limitations in production and transportation, for example, the tower diameter is limited to 4.3 m to meet the requirements of overpass heights of highway lines [9,10]. It means that the bending stiffness does not increase proportionally due to the limitations in transportation and manufacturing as the tower height increases, resulting in the decrease of the fundamental frequency. In consequence, the high tubular steel tower may

experience severe vibration [11]. Some new and innovative alternative tower concepts [12-15] have been proposed to overcome the limitations. One alternative approach is to construct the steel-concrete hybrid tower (SCHT), as shown in Fig. 1, which consists of several lower hollow concrete segments with prestressing force and upper tubular steel segments [16,17]. A concrete segment can be divided into several assembling parts and each part is prefabricated separately, which means that the diameter of the concrete segment can be much larger than that of the steel segment. Recently, a lightweight engineered cementitious composite (ECC) was developed to serve as protective coatings on the tall concrete towers, which can improve the durability performance of the concrete towers without compromising the towers' structural performance [18,19]. Therefore, it will be more effective to construct the SCHT to offer sufficient strength and stiffness for supporting wind turbines with increasing size and mass.

(a) Shanghai Electric Group. (b) Huadong Engineering Corporation.

Fig. 1 On-site photos of concrete-steel hybrid tower in China.

The fundamental frequency is a vital parameter affecting the dynamic response of

the structure. When the frequency of the applied load becomes close to the fundamental frequency, the structure resonance may occur. It means that the dynamic amplification factor of the structure will tend to be its maximum value, producing a violent dynamic response [20-22]. Therefore, in the structure design, the fundamental frequency of the structure must be kept away from the frequency ranges where resonance may occur. For the wind turbine tower, the frequency ranges causing the structure resonance include the rotor frequency (f_{1p}) and the blade passing frequency (f_{3p}), and the permissible fundamental frequency lies between f_{1p} and f_{3p} [23,24]. For a three-bladed turbine, which is the most common horizontal axis wind turbine, it has $f_{3p} = 3 \cdot f_{1p}$. The operational rotor speed of the MW-level wind turbine is about 6.9 to 12.1 revolutions per minute [25], which means that the range of rotor frequency f_{1p} is 0.115 Hz~0.202 Hz, and the range of blade passing frequency f_{3p} is 0.345 Hz~0.606 Hz. Fig. 2 shows the range of permissible frequency considering a relative deviation of $\pm 10\%$, where V_{max} and V_{min} denote the maximum and minimum rotor speed, respectively. Based on the above analysis, the fundamental frequency lying in the range of [0.222 Hz, 0.310 Hz] is feasible for the tower supporting the MW-level wind turbine.

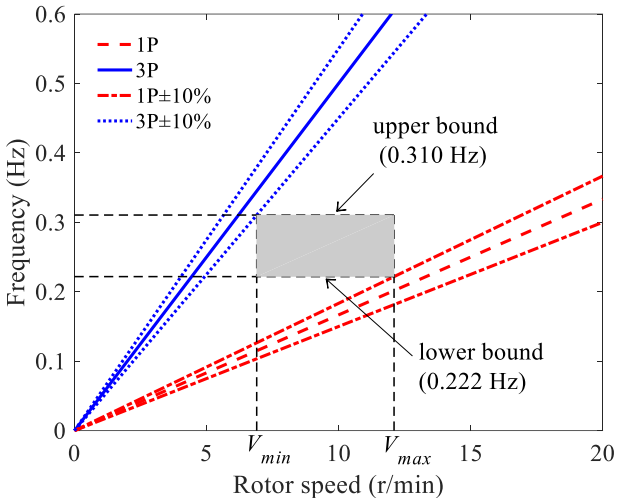

Fig. 2 Range of permissible frequency.

Different from the conventional tubular steel tower, the SCHT is composed of two different construction materials, and its cross-section size suddenly changes at the joint connecting the steel segment and the concrete segment, which leads to the complex structural configuration of the SCHT. Therefore, the structure analysis of the SCHT is mainly carried out through the finite element method (FEM) [26-30], and the related theoretical researches are still insufficient. Although FEM can offer accurate results about the static and dynamic response of the structure, the FE models might need to be reestablished when the configuration is adjusted, which makes FEM inefficient to be conducted in the preliminary design. On the other hand, the analytical method can offer an efficient way to obtain the fundamental frequency of the SCHT, and it also can be employed to investigate the variation rules of the fundamental frequency to the design parameters. Therefore, it is necessary to obtain the analytical method to calculate the fundamental frequency of the SCHT.

Previous studies on the fundamental frequency of wind turbine towers [31-34] are mainly for the tubular steel tower. Vugts [31] and Tempel [32] regarded the wind turbine

tower as a constant cross-section cantilever beam with a lumped mass at its free end and obtained the approximate expression for calculating the fundamental frequency of the tubular steel tower. In general, the wind turbine tower was tapered, and its diameter decreased with the increase in height. To consider the influence of taper on the fundamental frequency, Yang et al [33] simplified the wind turbine tower to a linearly tapered cantilever beam with a lumped mass at its free end and put forward a simplified method for calculating the fundamental frequency of the tubular steel tower based on the Rayleigh-Ritz method. Based on the transfer matrix method of multibody system, Gu et al [34] established a multi-body dynamics model of wind turbine tower system. The existing analytical solutions are derived based on the characteristics that the material properties of the tower remain unchanged and the dimensions of cross-section vary linearly with the increase of height. However, those characteristics are inapplicable for the SCHT. As illustrated in Fig. 3, the material properties and the cross-section dimensions change suddenly at the connection joints between the adapter ring and the steel/concrete segment, resulting in discontinuity of bending stiffness and mass along the tower length. In addition, to restrain the crack generation and fully display the superior compressive performance of concrete, the prestress is applied by arranging post-tensioning strands along with the concrete segments, which also has an impact on the fundamental frequency of the structure [35-37]. Therefore, the existing analytical solutions to the fundamental frequency of the wind turbine tower are no longer applicable to the SCHT. In Ref. [38], Huang et al solved the transverse free vibration equations of the SCHT by using the differential quadrature method [39,40] and obtained

the fundamental frequency of a numerical example. Despite this, the analytical solution for calculating the fundamental frequency of SCHT is still lacking in the investigation.

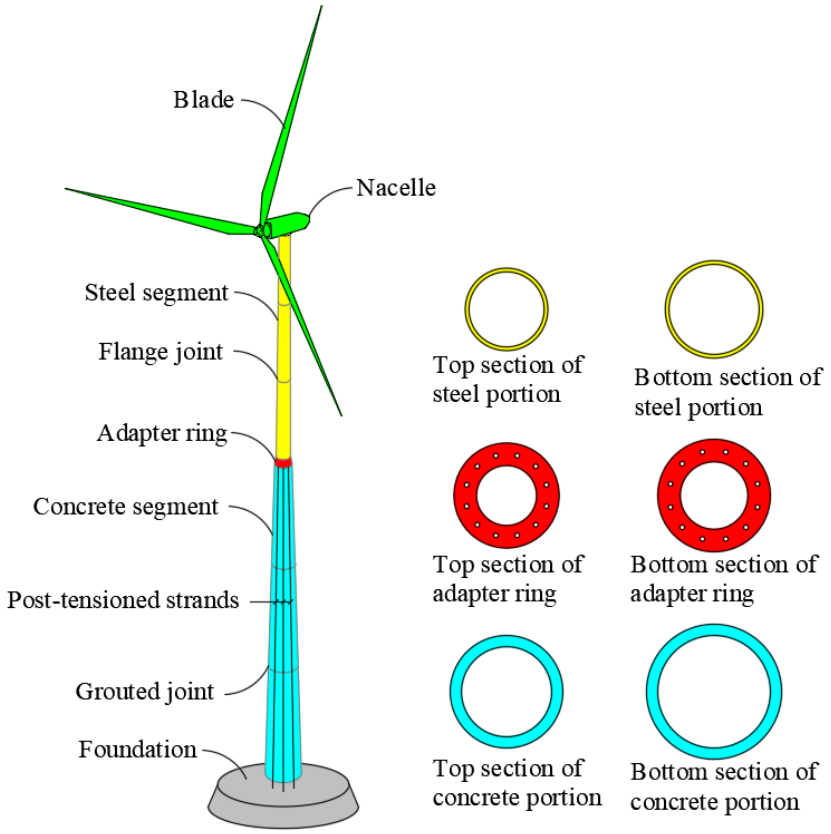

Fig. 3 Conceptual drawing of steel-concrete hybrid tower.

This study aims to obtain a closed-form solution of the fundamental frequency of the SCHT through theoretical derivation, taking into consideration the changes of cross-section dimensions and material properties of the tower along its length and the prestress applied along the concrete portion. By comparing the results of the proposed solution with the simulation results from FEM, the proposed solution is proved to be effective and accurate. In addition, a parametric analysis is conducted to investigate the correlation between the fundamental frequency and different design parameters, so as to provide the guidelines for the preliminary design of the SCHT.

2. Theoretical derivation

2.1 Transverse vibration equation

Considering a steel-concrete hybrid wind turbine tower, as shown in Fig. 3, consisting of the upper wind turbine, the steel portion, the adapter ring, and the concrete portion. D_{1b}, D_{2b}, and D_{3b} respectively denote the outer diameter of the bottom section of the concrete portion, the adapter ring, and the steel portion. Correspondingly, D_{1t}, D_{2t}, and D_{3t} denote the outer diameter at the top section of each portion, and h_1, h_2, and h_3 denote the length of each portion. For the SCHT, the concrete base diameter is within 10 m and the length is usually over 100 m [38]. The relatively large ratio of height to diameter makes the shear effect of the tower under the action of the transverse load inapparent. Besides, the upper wind turbine, including the nacelle and blades, can be regarded as a lumped mass. Therefore, the wind turbine tower is simplified as an Euler-Bernoulli beam with a lumped mass at its free end, as shown in Fig. 4, where *o* denotes the origin of the coordinates system, u and x denote the transverse and longitudinal coordinates respectively, $u(x, t)$ denotes the transverse displacement of the hybrid tower, which continuously varies with longitudinal coordinate x and time t, d denotes the distance from the centroid of the wind turbine to the top end of the tower. According to the transverse vibration theory of Euler-Bernoulli beam [20], the transverse free vibration equation of the hybrid tower can be written as

$$M(x)\frac{\partial^2 u(x,t)}{\partial t^2}+\frac{\partial^2}{\partial x^2}\left[K(x)\frac{\partial^2 u(x,t)}{\partial x^2}\right]=0\,, \tag{1}$$

where $K(x)$ denotes the function of bending stiffness, and $M(x)$ denotes the function of mass per unit length.

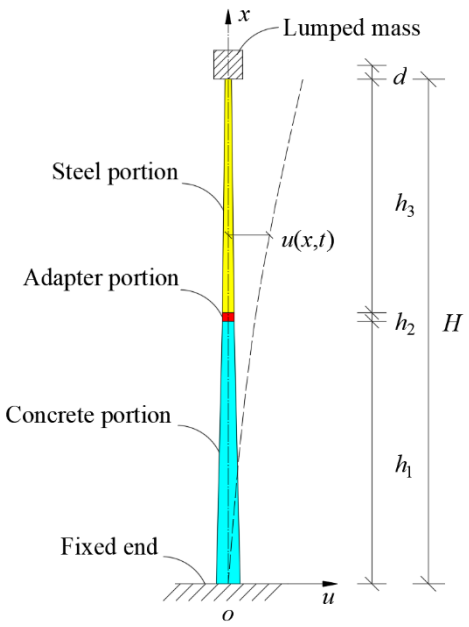

Fig. 4 Simplified configuration of steel-concrete hybrid tower.

For an onshore wind turbine tower, it is usually supported on a huge reinforced concrete plinth with piles attached, which leads to the fact that the soil-structures interaction can be ignored in the design [41]. Therefore, it is reasonable to consider the foundation as fixed. The boundary conditions at the bottom end are

$$u(0,t)=0, \tag{2}$$

$$\frac{\partial u}{\partial x}(0,t)=0. \tag{3}$$

As shown in Fig. 5, the lumped mass is taken as the isolated body to analyze the boundary conditions at the top end, where m_{wt} and J_{wt} denote the mass and rotary inertia of the wind turbine, respectively.

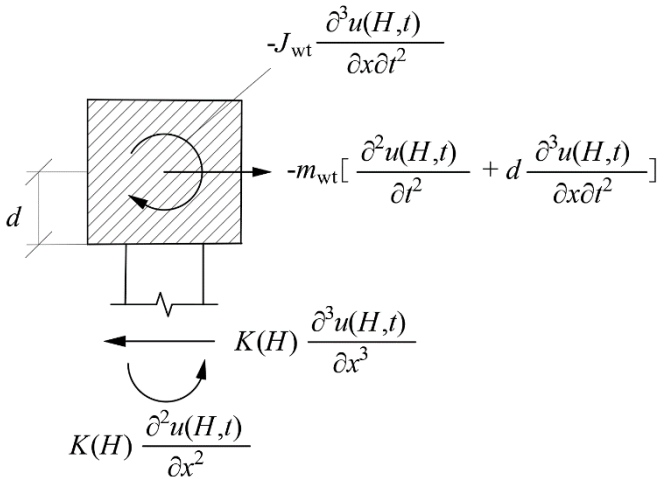

Fig. 5 Force analysis of the isolated body.

From the equilibrium conditions of force and moment acting on the lumped mass, it can be deduced that the boundary conditions to be satisfied at the top end of SCHT are

$$K(H)\frac{\partial^3 u}{\partial x^3}(H,t)=-m_{wt}\left[\frac{\partial^2 u(H,t)}{\partial t^2}+d\frac{\partial^3 u(H,t)}{\partial x\partial t^2}\right], \tag{4}$$

$$K(H)\frac{\partial^2 u}{\partial x^2}(H,t)=-\frac{\partial^3 u(H,t)}{\partial x\partial t^2}\left(J_{wt}+m_{wt}d^2\right)-\frac{\partial^2 u(H,t)}{\partial t^2}m_{wt}d\ . \tag{5}$$

Since the cross-section dimensions and material properties of the hybrid tower vary along longitudinal coordinate x, it is appropriate to describe $M(x)$ and $K(x)$ by piecewise functions. Let E_1, E_2, and E_3 respectively denote the modulus of elasticity of the concrete portion, the adapter ring, and the steel portion. Correspondingly, ρ_1, ρ_2, and ρ_3 denote the mass density of each portion, and t_1, t_2, and t_3 denote the thickness of each portion. Then, $M(x)$ and $K(x)$ can be expressed as

$$M(x)=\begin{cases} m_{10}+m_{11}x, & 0\le x<h_1 \\ m_{20}+m_{21}(x-h_1), & h_1\le x\le h_1+h_2 \\ m_{30}+m_{31}(x-h_1-h_2), & h_1+h_2<x\le h_1+h_2+h_3 \end{cases}, \tag{6}$$

$$K(x)=\begin{cases}\sum_{i=0}^{3}k_{1i}x^{i}, & 0\le x<h_1\\ \sum_{i=0}^{3}k_{2i}\left(x-h_1\right)^{i}, & h_1\le x\le h_1+h_2\\ \sum_{i=0}^{3}k_{3i}\left(x-h_1-h_2\right)^{i}, & h_1+h_2<x\le h_1+h_2+h_3\end{cases}, \tag{7}$$

where

$$m_{i0}=\frac{\pi}{4}\rho_i\left[D_i^2-\left(D_i-2t_i\right)^2\right], \tag{8}$$

$$m_{i1}=\frac{\pi}{2}\rho_i\left(\frac{D_{ib}-D_{it}}{h_i}\right)\left[\left(D_i-2t_i\right)-D_i\right], \tag{9}$$

$$k_{i0}=\frac{\pi}{64}E_i(D_i^4-\left(D_i-2t_i\right)^4), \tag{10}$$

$$k_{i1}=\frac{\pi}{16}E_i\left[\left(D_i-2t_i\right)^3-D_i^3\right]\left(\frac{D_{ib}-D_{it}}{h_i}\right), \tag{11}$$

$$k_{i2}=\frac{3\pi}{32}E_i\left[D_i^2-\left(D_i-2t_i\right)^2\right]\left(\frac{D_{ib}-D_{it}}{h_i}\right)^2, \tag{12}$$

$$k_{i3}=\frac{\pi}{16}E_i\left[\left(D_i-2t_i\right)-D_i\right]\left(\frac{D_{ib}-D_{it}}{h_i}\right)^3. \tag{13}$$

2.2 Derivation of vibration frequency

The transverse free vibration equation of the hybrid tower, Eq. (1), is a partial differential equation with variable coefficients, and the coefficients are discontinuous functions, making it difficult to analytically solve Eq. (1) by elementary methods. This section presents a detailed analysis of the kinetic energy and the potential energy of the SCHT, where the influence of m_{wt}, J_{wt}, and prestressing force are taken into consideration. Then, a frequency equation of the SCHT is established based on the Rayleigh-Ritz method [20], from which the natural frequencies and the corresponding

vibration modes can be obtained.

The kinetic energy of the SCHT comes from two aspects, including the one of the SCHT itself and the one of the wind turbine. As depicted in Fig. 6, a segment of a microelement with a length of dx is cut from the tower. The mass and velocity in the lateral direction of the microelement are $M(x)\mathrm{d}x$ and $\partial u(x,t)/\partial t$, respectively. Then, the kinetic energy of this microelement, which is denoted by $\mathrm{d}T_1(t)$, can be expressed as

$$\mathrm{d}T_1(t)=\frac{1}{2}M(x)\left[\frac{\partial u(x,t)}{\partial t}\right]^2\mathrm{d}x. \tag{14}$$

Integrating the above formula within the interval [0, H] yields the kinetic energy of the whole tower

$$T_1(t)=\frac{1}{2}\int_0^H M(x)\left[\frac{\partial u(x,t)}{\partial t}\right]^2\mathrm{d}x. \tag{15}$$

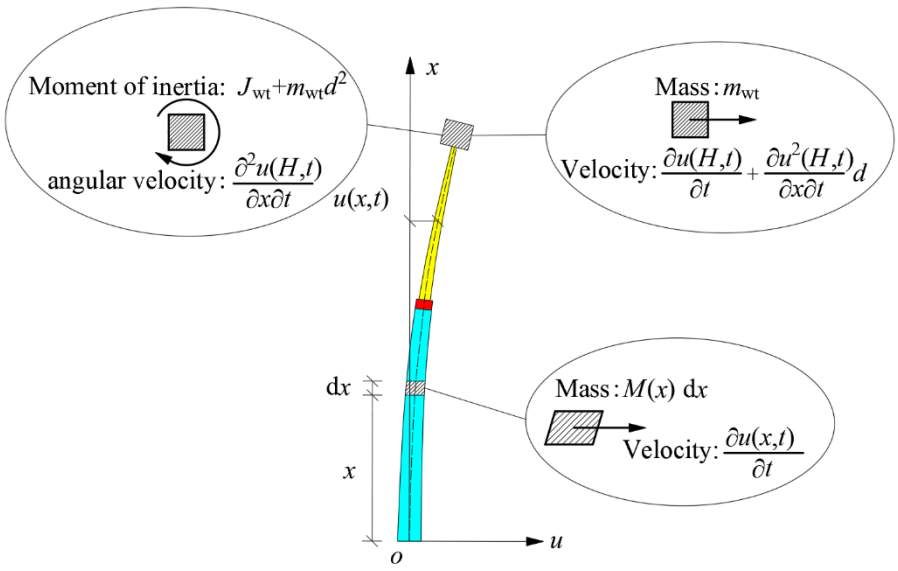

Fig. 6 Kinetic energy analysis of SCHT.

The kinetic energy of the wind turbine can be expressed as

$$T_2(t)=\frac{1}{2}m_{\mathrm{wt}}v_1^2+\frac{1}{2}\left(J_{\mathrm{wt}}+m_{\mathrm{wt}}d^2\right)w_1^2, \tag{16}$$

where v_1 and w_1 denote the velocity of the wind turbine at its centroid and the angular velocity of the tower at its top end, respectively. The expressions of v_1 and w_1 are as follows

$$v_1=\left.\frac{\partial u(x,t)}{\partial t}\right|_{x=H}+d\left.\frac{\partial^2 u(x,t)}{\partial x\partial t}\right|_{x=H}, \tag{17}$$

$$w_1=\left.\frac{\partial^2 u(x,t)}{\partial x\partial t}\right|_{x=H}. \tag{18}$$

Substituting Eqs. (17) and (18) into Eq. (16) yield the kinetic energy of the wind turbine. The kinetic energy of the whole structure is

$$\begin{aligned}T(t)=&\frac{1}{2}\int_0^H M(x)\left[\frac{\partial u(x,t)}{\partial t}\right]^2\mathrm{d}x+\frac{1}{2}m_{\mathrm{wt}}\left[\left.\frac{\partial u(x,t)}{\partial t}\right|_{x=H}+d\left.\frac{\partial^2 u(x,t)}{\partial x\partial t}\right|_{x=H}\right]^2\\&+\frac{1}{2}\left(J_{\mathrm{wt}}+m_{\mathrm{wt}}d^2\right)\left[\left.\frac{\partial^2 u(x,t)}{\partial x\partial t}\right|_{x=H}\right]^2\end{aligned}. \tag{19}$$

In practical engineering, the upper ends of the steel strands are anchored at the top of the adapter ring, and the anchor points of the lower ends are located in the internal cavity of the foundation, making it unable to form a self-equilibrium system between the hybrid tower and the steel strands. Therefore, the prestress effect applied by the steel strands is simplified as the axial external force acting on the top surface of the adapter ring. Since the locations of the adapter ring and the wind turbine vary during the vibration, the work done by the axial force and the gravity of the wind turbine would affect the potential energy of the SCHT. It has

$$U=U_1+U_2+U_3, \tag{20}$$

where U denotes the potential energy of the system, U_1 denotes the bending strain

energy, U_2 and U_3 denote the work done by the axial force and the gravity of the wind turbine. The bending strain energy U_1 can be written as

$$U_1 = \frac{1}{2}\int_0^H K(x)\left[\frac{\partial u^2(x,t)}{\partial x^2}\right]^2 \mathrm{d}x\,. \tag{21}$$

To obtain the expressions of U_2 and U_3, starting from the transverse deformation of the concrete portion, the displacement of the acting position of axial force is studied. As shown in Fig. 7, a segment of a microelement $\overline{AB}$ with a length of dx is cut from the undeflected tower, where P denotes the axial force. When the tower is deflected, the microelement $\overline{AB}$ became $A'B'$, and the vertical displacement of the top end of the microelement is

$$\delta = (1-\cos\theta)\mathrm{d}x\,, \tag{22}$$

where θ denotes the included angle between $\overline{AB}$ and $A'B'$.

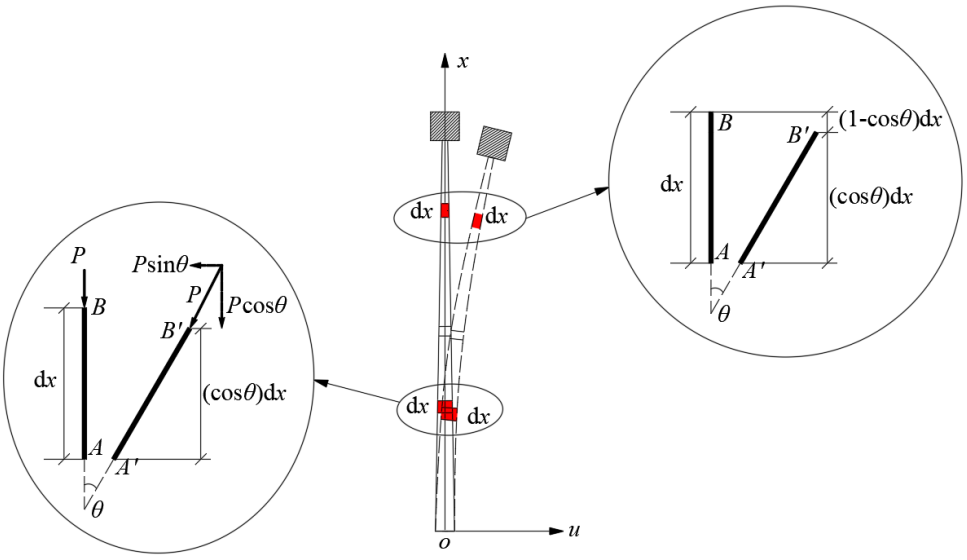

Fig. 7 Potential energy analysis of SCHT.

Suppose that the microelement is cut from the concrete portion, it is under the action of the axial force P. The component of the axial force P along the direction of the x-axis is $P\cdot\cos\theta$. Then, the work dW_{pre} done by the axial force P on the microelement

segment with a length of dx is

$$\mathrm{d}W_{\mathrm{pre}} = P \cdot \cos\theta \cdot \delta . \tag{23}$$

Since θ is infinitesimal, according to the theorem of equivalent infinitesimal replacement, it has

$$P \cdot \cos\theta \sim P , \tag{24}$$

$$1 - \cos\theta \sim \frac{1}{2}\theta^2 , \tag{25}$$

$$\theta \sim \tan\theta = \frac{\partial u(x,t)}{\partial x} . \tag{26}$$

Substituting Eqs. (24)-(26) into Eqs. (22) and (23), it yields

$$\delta = \frac{1}{2}\left[\frac{\partial u(x,t)}{\partial x}\right]^2 \mathrm{d}x , \tag{27}$$

$$\mathrm{d}W_{\mathrm{pre}} = P \cdot \frac{1}{2}\left[\frac{\partial u(x,t)}{\partial x}\right]^2 \mathrm{d}x . \tag{28}$$

Eqs. (27) and (28) are integrated within the intervals $[0, H]$ and $[0, h_1+h_2]$, respectively, yielding the vertical displacement of the wind turbine and work done by the axial force P during the vibration of the SCHT

$$\Delta = \int_0^H \left[\frac{\partial u(x,t)}{\partial x}\right]^2 \mathrm{d}x , \tag{29}$$

$$W_{\mathrm{pre}} = \frac{P}{2}\int_0^{h_1+h_2} \left[\frac{\partial u(x,t)}{\partial x}\right]^2 \mathrm{d}x . \tag{30}$$

The work done by the gravity of the wind turbine is

$$W_{\mathrm{wt}} = \frac{1}{2} m_{\mathrm{wt}} g \int_0^H \left[\frac{\partial u(x,t)}{\partial x}\right]^2 \mathrm{d}x , \tag{31}$$

where g denotes the acceleration of gravity. Since both the W_{wt} and W_{pre} are positive, then the increase of the potential energy is negative. The total potential energy of the hybrid tower is

$$U(t)=\frac{1}{2}\int_0^H K(x)\left[\frac{\partial u^2(x,t)}{\partial x^2}\right]^2 \mathrm{d}x-\frac{P}{2}\int_0^{h_1+h_2}\left[\frac{\partial u(x,t)}{\partial x}\right]^2 \mathrm{d}x -\frac{m_{\mathrm{wt}}g}{2}\int_0^H\left[\frac{\partial u(x,t)}{\partial x}\right]^2 \mathrm{d}x \tag{32}$$

The transverse displacement of the hybrid tower can be expressed as

$$u(x,t)=y(x)\sin(\omega t+\varphi), \tag{33}$$

where $y(x)$ denotes the vibration mode, ω and φ denote the natural frequency and vibration phrase, respectively.

Substituting Eq. (33) into Eqs. (19) and (32), it yields

$$T(t)=\frac{1}{2}\omega^2\cos^2(\omega t+\varphi)\left\{\begin{array}{l}\int_0^H M(x)\left[y(x)\right]^2 \mathrm{d}x+\left[y(H)+y'(H)d\right]^2\\ +\left(J_{\mathrm{wt}}+m_{\mathrm{wt}}d^2\right)\left[y'(H)\right]^2\end{array}\right\}, \tag{34}$$

$$U(t)=\frac{1}{2}\sin^2(\omega t+\varphi)\left\{\begin{array}{l}\int_0^H K(x)\left[y''(x)\right]^2 \mathrm{d}x-P\int_0^{h_1+h_2}\left[y'(x)\right]^2\mathrm{d}x\\ -m_{\mathrm{wt}}g\int_0^H\left[y'(x)\right]^2\mathrm{d}x\end{array}\right\}. \tag{35}$$

On the one hand, the kinetic energy reaches its maximum when $t=(n\pi-\varphi)/\omega$, meanwhile the potential energy becomes zero. On the other hand, when t takes $[(2n+1)\pi/2-\varphi]/\omega$, the kinetic energy is zero, while the potential energy reaches its maximum. The maximum values of $T(t)$ and $U(t)$ can be expressed as

$$T_{\max}=\frac{1}{2}\omega^2\left\{\begin{array}{l}\int_0^H M(x)\left[y(x)\right]^2 \mathrm{d}x+m_{\mathrm{wt}}\left[y(H)+y'(H)d\right]^2\\ +\left(J_{\mathrm{wt}}+m_{\mathrm{wt}}d^2\right)\left[y'(H)\right]^2\end{array}\right\}, \tag{36}$$

$$U_{\max}=\frac{1}{2}\left\{\begin{array}{l}\int_0^H K(x)\left[y''(x)\right]^2 \mathrm{d}x-P\int_0^{h_1+h_2}\left[y'(x)\right]^2\mathrm{d}x\\ -m_{\mathrm{wt}}g\int_0^H\left[y'(x)\right]^2\mathrm{d}x\end{array}\right\}. \tag{37}$$

According to the law of energy conservation, the mechanical energy of a conservation system remains unchanged when the system vibrates at a certain

frequency [20], that is

$$T(t)+U(t)=C, \tag{38}$$

where $T(t)$ and $U(t)$ denote the kinetic and potential energy of the system at a certain time, respectively, and C is a constant. Therefore, it has

$$U_{\max}=T_{\max}. \tag{39}$$

A linear combination of a set of independent coordinate functions is used as the approximate expression of the vibration mode $y(x)$

$$y(x)\cong\sum_{i=0}^{n}q_i\phi_i(x) \tag{40}$$

where q_i are undetermined constants, coordinate functions $\phi_i(x)$ satisfy the geometry boundary conditions of the SCHT, which is usually called displacement function.

Since Eq. (40) is an approximate expression, it means that Eq. (39) is not tenable when adopting Eq. (40) as the vibration mode. It constructs the following function

$$\Pi=U_{\max}-T_{\max}. \tag{41}$$

Substituting Eq. (39) into Eqs. (35), (36), and (40), it has

$$\begin{aligned}\Pi=&\frac{1}{2}\left\{\begin{array}{l}\displaystyle\int_0^H K(x)\left[\sum_{i=0}^{n}q_i\phi_i''(x)\right]^2\mathrm{d}x-P\int_0^{h_1+h_2}\left[\sum_{i=0}^{n}q_i\phi_i'(x)\right]^2\mathrm{d}x\\ \displaystyle -m_{\mathrm{wt}}g\int_0^H\left[\sum_{i=0}^{n}q_i\phi_i'(x)\right]^2\mathrm{d}x\end{array}\right\}\\ &-\frac{1}{2}\omega^2\left\{\begin{array}{l}\displaystyle\int_0^H M(x)\left[\sum_{i=0}^{n}q_i\phi_i(x)\right]^2\mathrm{d}x+\left(J_{\mathrm{wt}}+m_{\mathrm{wt}}d^2\right)\left[\sum_{i=0}^{n}q_i\phi_i'(x)\Big|_{x=H}\right]^2\\ \displaystyle +m_{\mathrm{wt}}\left[\sum_{i=0}^{n}q_i\phi_i(H)+d\sum_{i=0}^{n}q_i\phi_i'(x)\Big|_{x=H}\right]^2\end{array}\right\},\end{aligned} \tag{42}$$

where Π is the difference between $U_{\max}$ and $T_{\max}$. It should be noted that Π is the function quadratic in q_i, and the closer Π is to zero, the closer ω is to the exact value.

The necessary conditions for Π to be minimized are that

$$\frac{\partial \Pi}{\partial q_i} = 0 . \tag{43}$$

By substituting Eq. (42) into Eq. (43), a set of homogeneous equations can be obtained, which has the form

$$\left(\mathbf{K} - \omega^2 \mathbf{M}\right)\mathbf{q} = \mathbf{0} , \tag{44}$$

where **K** and **M** denote the stiffness matrix and mass matrix of the SCHT, **q** is a vector composed of undetermined constants q_i.

The necessary and sufficient condition for Eq. (44) to have non-zero solutions is that the coefficient determinant is zero, that is

$$\left|\mathbf{K} - \omega^2 \mathbf{M}\right| = 0 . \tag{45}$$

An equation of ω can be obtained after expanding the determinant in Eq. (45), which is called the frequency equation of the SCHT. Theoretically, the first n+1 orders of natural frequencies can be obtained by solving the obtained equation

$$\omega_1 < \omega_2 < \omega_3 < \cdots \omega_{n+1} . \tag{46}$$

Taking the damping into consideration, the expression of natural frequency f is

$$f = \frac{\omega}{2\pi} \cdot \sqrt{1 - \xi^2} , \tag{47}$$

where ξ denotes the damping ratio of the wind turbine tower, including the aerodynamic damping ratio and structural damping ratio. Substituting the natural frequency ω_i into the homogeneous equations (Eq. (44)), the value of q_i (i=0,1,2,…,n) can thus be obtained. Then, q_i and $\phi_i(x)$ are further substituted into Eq. (40), which forms the vibration mode y_i corresponding to each ω_i.

Substituting the obtained vibration mode y_i into Eqs. (36) and (37), and making

the following definition:

$$M_{\mathrm{eq}}^{(i)}=\int_0^H M(x)\left[y_i(x)\right]^2\mathrm{d}x+m_{\mathrm{wt}}\left[y_i(H)+y_i'(H)d\right]^2 +\left(J_{\mathrm{wt}}+m_{\mathrm{wt}}d^2\right)\left[y_i'(H)\right]^2, \tag{48}$$

$$K_{\mathrm{eq}}^{(i)}=\int_0^H K(x)\left[y_i''(x)\right]^2\mathrm{d}x-P\int_0^{h_1+h_2}\left[y_i'(x)\right]^2\mathrm{d}x -m_{\mathrm{wt}}g\int_0^H\left[y_i'(x)\right]^2\mathrm{d}x. \tag{49}$$

Then, the natural frequency can also be expressed as

$$f_i=\frac{\sqrt{1-\xi^2}}{2\pi}\cdot\sqrt{\frac{K_{\mathrm{eq}}^{(i)}}{M_{\mathrm{eq}}^{(i)}}}, \tag{50}$$

where $M_{\mathrm{eq}}^{(i)}$ and $K_{\mathrm{eq}}^{(i)}$ denote the equivalent mass per unit length and bending stiffness, respectively.

2.3 Construction of displacement function

In this section, a set of Gram-Schmidt orthogonal polynomials [42-44] is used to construct the displacement function of the SCHT, which has the form of

$$\phi_1(x)=\frac{(x-B_1)\phi_0(x)}{\sqrt{\int_0^H\left[(x-B_1)\phi_0(x)\right]^2\mathrm{d}x}}, \tag{51}$$

$$\phi_k(x)=\frac{(x-B_k)\phi_{k-1}(x)-C_k\phi_{k-2}(x)}{\sqrt{\int_0^H\left[(x-B_k)\phi_{k-1}(x)-C_k\phi_{k-2}(x)\right]^2\mathrm{d}x}}, \tag{52}$$

$$B_k=\frac{\int_0^H x\phi_{k-1}^2(x)\mathrm{d}x}{\int_0^H\phi_{k-1}^2(x)\mathrm{d}x}, \tag{53}$$

$$C_k=\frac{\int_0^H x\,\phi_{k-1}(x)\phi_{k-2}(x)\mathrm{d}x}{\int_0^H\phi_{k-2}^2(x)\mathrm{d}x}, \tag{54}$$

where $\phi_0(x)$ is the first polynomial. The polynomials $\phi_k(x)$ satisfy the orthogonality condition

$$\int_0^H \phi_k(x)\phi_l(x)\mathrm{d}x = \begin{cases} 0 & k \neq l \\ 1 & k = l \end{cases}. \tag{55}$$

It is noted that if $\phi_0(x)$ satisfies the geometric boundary condition (Eqs. (2) and (3)), then the other members of the orthogonal set also satisfy the geometric boundary condition, which can be checked from Eq. (51)~Eq. (54). Therefore, the necessary condition of constructing the first member polynomial $\phi_0(x)$ is to satisfy the geometric boundary conditions of the SCHT.

3. Error analysis

3.1 Numerical example

One SCHT with a top mass of 250 tons and pretension force of 48 MN is applied as a numerical example, its dimensions are listed in Table 1.

Table 1 Dimensions of numerical example.

	Concrete portion	Adapter ring	Steel portion
Length (mm)	60000	2000	60000
Thickness (mm)	300	1600	30
Top diameter (mm)	5000	4600	3300
Bottom diameter (mm)	7000	5000	4000

As shown in Fig. 8, the wind turbine is mainly composed of nacelle, blades, and hub. To facilitate the description of the parameters, a three-dimensional rectangular coordinate system is established, where the coordinate origin *o* is located at the centroid of the wind turbine, the *y*-axis is in the windward direction of the blades, the *z*-axis is in the direction of the tower axis, and the *x*-axis is perpendicular to the *y*-*z* plane. Table 2 lists the main parameters of the wind turbine, where J_x and J_y denote the rotary inertia of the wind turbine about the *x*-axis and *y*-axis, respectively.

Table 2 Main parameters of wind turbine

Blade diameter	Hub diameter	Nacelle dimension	Total mass	d	J_x (kg·m^2)	J_y (kg·m^2)
120 m	5 m	13m×5m×5.6m	250 t	2.8 m	4.23×10^7	7.47×10^7

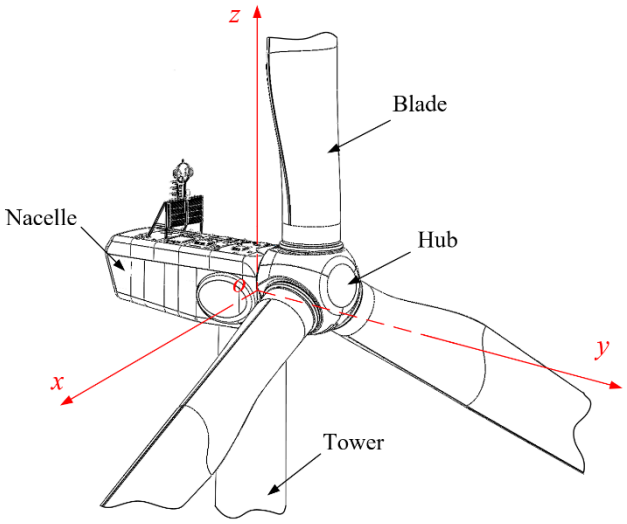

Fig. 8 Schematic of wind turbine.

3.2 Development of FE model

As shown in Fig. 9, the FE model included five parts: concrete portion, adapter ring, steel portion, wind turbine, and steel strand. The concrete portion and wind turbine were modeled by 8-node linear brick elements with reduced integration (C3D8R), while the adapter ring was modeled by 10-node quadratic tetrahedral elements (C3D10) with better grid adaptability because some holes were set in the adapter ring to make it possible for steel strands to pass through. The steel portion was modeled by 4-node curved shell elements with reduced integration (S4R), and the steel strand was modeled by 2-node linear 3-D truss elements (T3D2). Concrete with C60 grade and C70 grade were used to define the concrete portion and adapter ring, respectively, the steel portion was defined by Q355 grade steel, and the grade of the steel strand was 1850. Specific material properties were listed in Table 3. It should be noted that the steel density was defined as 8500 kg/m^3 rather than the typical value of 7850kg/m^3 to consider the

influence of paint and connections [45]. The coefficient of linear expansion of the steel strand, which was definite to simulate the effect of prestressing with the method of cooling temperature [46,47], was also listed in Table 2. All fixed connections, including the connections between the concrete portion and the adapter ring, the steel portion and the adapter ring, as well as the steel portion and wind turbine, were simulated by tie constraints. The top end of each steel strand was coupled with the periphery of each hole at the top of the adapter ring, and the bottom end of each steel strand was pinned by restraining all translational degrees of freedom. The bottom end of the concrete portion was fixed by restraining all translational and rotational degrees of freedom. The vibration modes of the FE model are shown in Fig. 10, where SS and AF represent the directions of side-to-side and after-to-front, respectively.

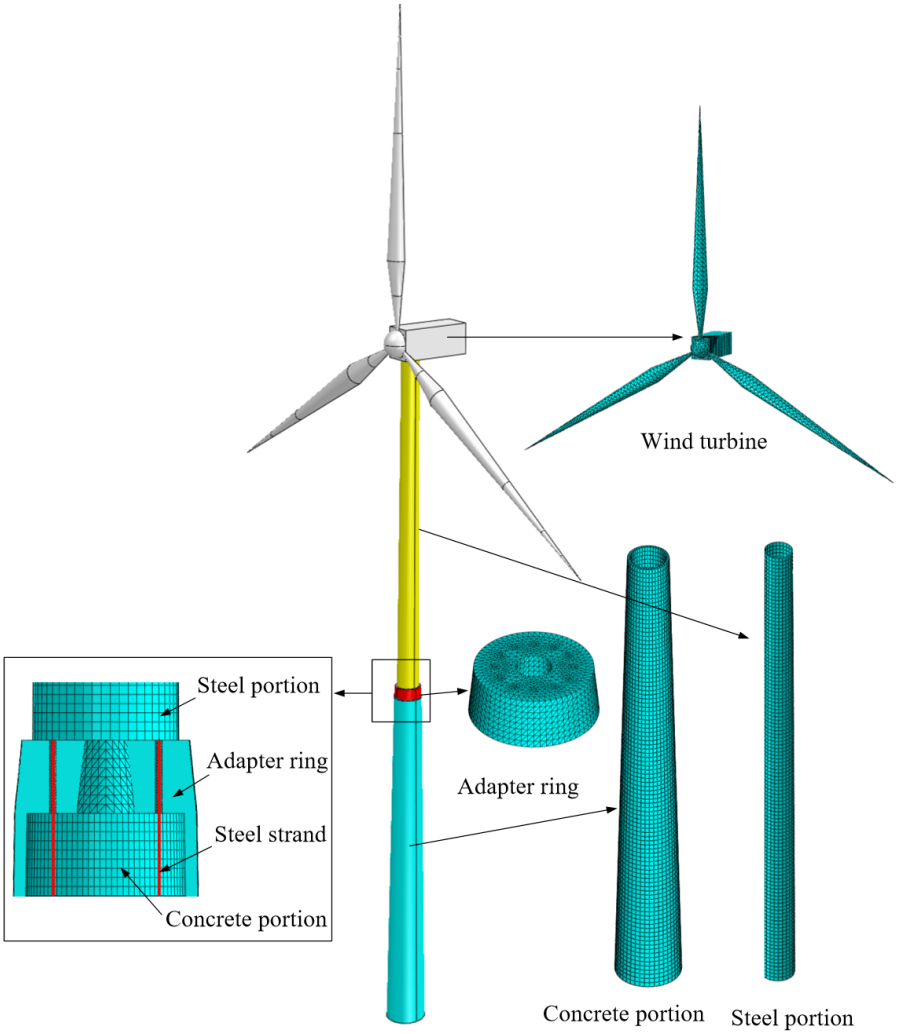

Fig 9 Finite element model of hybrid tower.

Table 3 Definitions of material properties.

Material	Density (kg/m^3)	Modulus of elasticity (MPa)	Poisson's ratio	Coefficient of linear expansion (1/℃)
C60 concrete	2500	36000	0.2	/
C70 concrete	2500	37000	0.2	/
Steel	8500	206000	0.3	/
Steel strand	7850	195000	0.3	1×10^{-5}

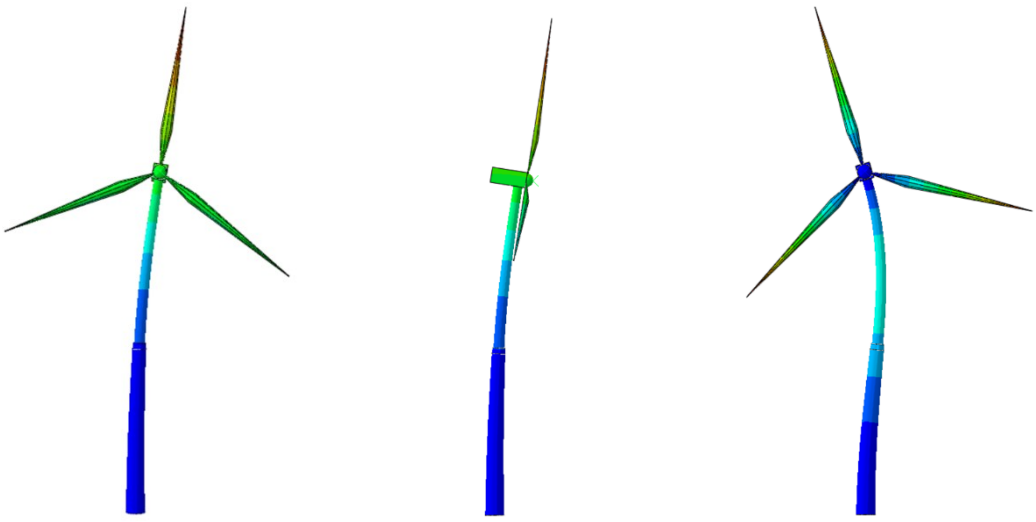

(a) Mode 1 SS. (b) Mode 1 FA. (c) Mode 2 SS.

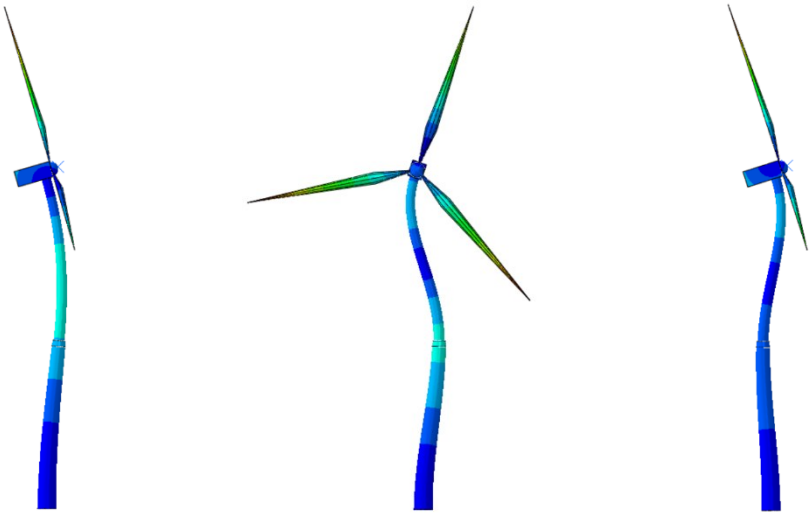

(d) Mode 2 FA. (e) Mode 3 SS. (f) Mode 3 AF.

Fig.10 First three vibration modes of SCHT.

To improve the efficiency of numerical simulation, mesh sensitivity analysis is carried out to determine the appropriate mesh size. The different mesh sizes of 1.5m, 1.0m, 0.5m, 0.25m, and 0.1m were used to divide the FE model, and the comparison was shown in Fig. 11. It can be seen that the numerical results were insensitive to the FE models with mesh sizes of 0.25m and 0.10m. To balance the computational efficiency and accuracy, a mesh size of 0.25 m was adopted for the FE model.

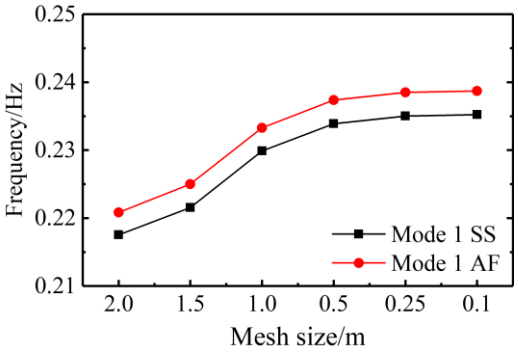

(a) Simulation of 1st order frequency.

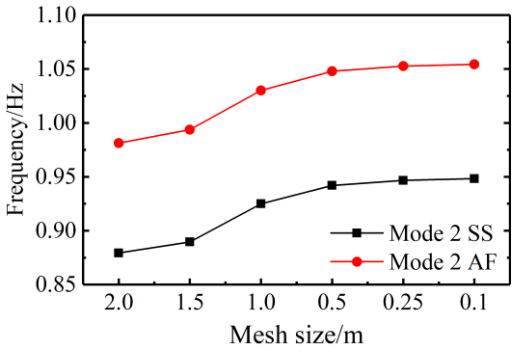

(b) Simulation of 2nd order frequency.

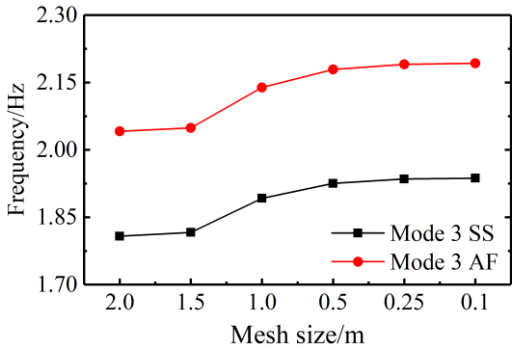

(c) Simulation of 3rd order frequency.

Fig 11 Sensitivity analysis of mesh size.

For the FE model with an elastic foundation, the bottom end of the concrete portion was fixed by restraining all translational degrees of freedom, while the rotational degrees of freedom were restrained by springs with rotational stiffness of $K_{\varphi,\mathrm{dyn}}$, where $K_{\varphi,\mathrm{dyn}}$ is calculated by the method in Ref. [48]. Table 4 lists the simulation results of the FE models with different foundation stiffnesses, where R_0 is the radius of the foundation, $E_{\mathrm{s,dyn}}$ and v are the dynamic compressive modulus and Poisson's ratio of the soil under the foundation, respectively, f is the fundamental frequency of the SCHT, $\xi_{\mathrm{f\text{-}e}}$ is the relative error between the results obtained with fixed and elastic foundations.

$$\xi_{\mathrm{f\text{-}e}} = \frac{f_{\mathrm{fixed}} - f_{\mathrm{elastic}}}{f_{\mathrm{fixed}}} \times 100\% , \tag{56}$$

where f_{fixed} (0.23502 Hz) and f_{elastic} denote the results obtained with fixed and elastic

foundations, respectively.

Table 4 Simulation results of the FE models with different dynamic rotational stiffness

Soil	R_0(m)	$E_{s,dyn}$(MPa)	ν	$K_{\varphi,dyn}$(N·m/rad)	f (Hz)	$\xi_{f\text{-}e}$
Gravel	10	600	0.2	7.50×10^{11}	0.23270	0.99%
Sand	10	400	0.25	5.93×10^{11}	0.23210	1.24%
Clay	10	300	0.25	4.74×10^{11}	0.23137	1.55%
Silt	10	200	0.3	3.27×10^{11}	0.22976	2.24%

It can be seen that the maximum relative error is 2.24%, while the minimum is only 0.99%. It indicates that foundation stiffness has a limited influence on the fundamental frequency of the SCHT. Besides, the calculation method in Ref. [48] has underestimated the foundation stiffness, since the contribution of piles is not considered. Therefore, it is reasonable to consider the foundation as fixed.

3.3 Convergence of solution

As can be seen from Section 2, the accuracy of the proposed solution is related to the form of the assumed vibration mode (Eq. (39)), including the number of polynomials and the first member of orthogonal polynomials. To study the influence of the assumed vibration mode on the results obtained with the proposed solution, the following curves are used to construct $\phi_0(x)$. They are

$$X(x)=6\left(\frac{x}{H}\right)^2-4\left(\frac{x}{H}\right)^3+\left(\frac{x}{H}\right)^4, \tag{57}$$

$$X(x)=3\left(\frac{x}{H}\right)^2-\left(\frac{x}{H}\right)^3, \tag{58}$$

$$X(x)=\left(\frac{x}{H}\right)^2, \tag{59}$$

$$X(x)=\left(\frac{x}{H}\right)^3. \tag{60}$$

Eq. (57) and Eq. (58) are the dimensionless deflection curves of a homogeneous

cantilever beam with length H under uniformly distributed load and concentrated force at its free end, respectively. Eq. (59) and Eq. (60) are the power functions satisfying geometric boundary conditions of SCHT. The first member of orthogonal polynomials $\phi_0(x)$ is obtained by normalizing the above curves

$$\phi_0(x) = \frac{X(x)}{\sqrt{\int_0^H X^2(x)\,\mathrm{d}x}}. \tag{61}$$

Fig. 12 shows the convergence trend of the first three orders natural frequencies. Table 5 lists the convergence results obtained from constructing $\phi_0(x)$ with Eq. (57)~Eq. (60), respectively, where s denotes the standard deviation of those results. It can be seen that the natural frequency decreases and tends to converge as the number of polynomials increases. It indicates that some differences exist between the assumed vibration mode and the real one, which is equivalent to adding additional constraints to the original structure, resulting in the overestimation of the natural frequency. Therefore, the proposed solution is the upper bound of the exact value. As can be seen in Table 5, the results obtained by constructing $\phi_0(x)$ with Eq. (57) are minimum, so Eq. (57) is the most suitable curve to construct $\phi_0(x)$ within the scope of this study. Besides, although the displacement functions generated with different curves that satisfy the geometric boundary conditions of SCHT have a certain impact on the convergence trend of the natural frequencies, the difference among the convergence results is little.

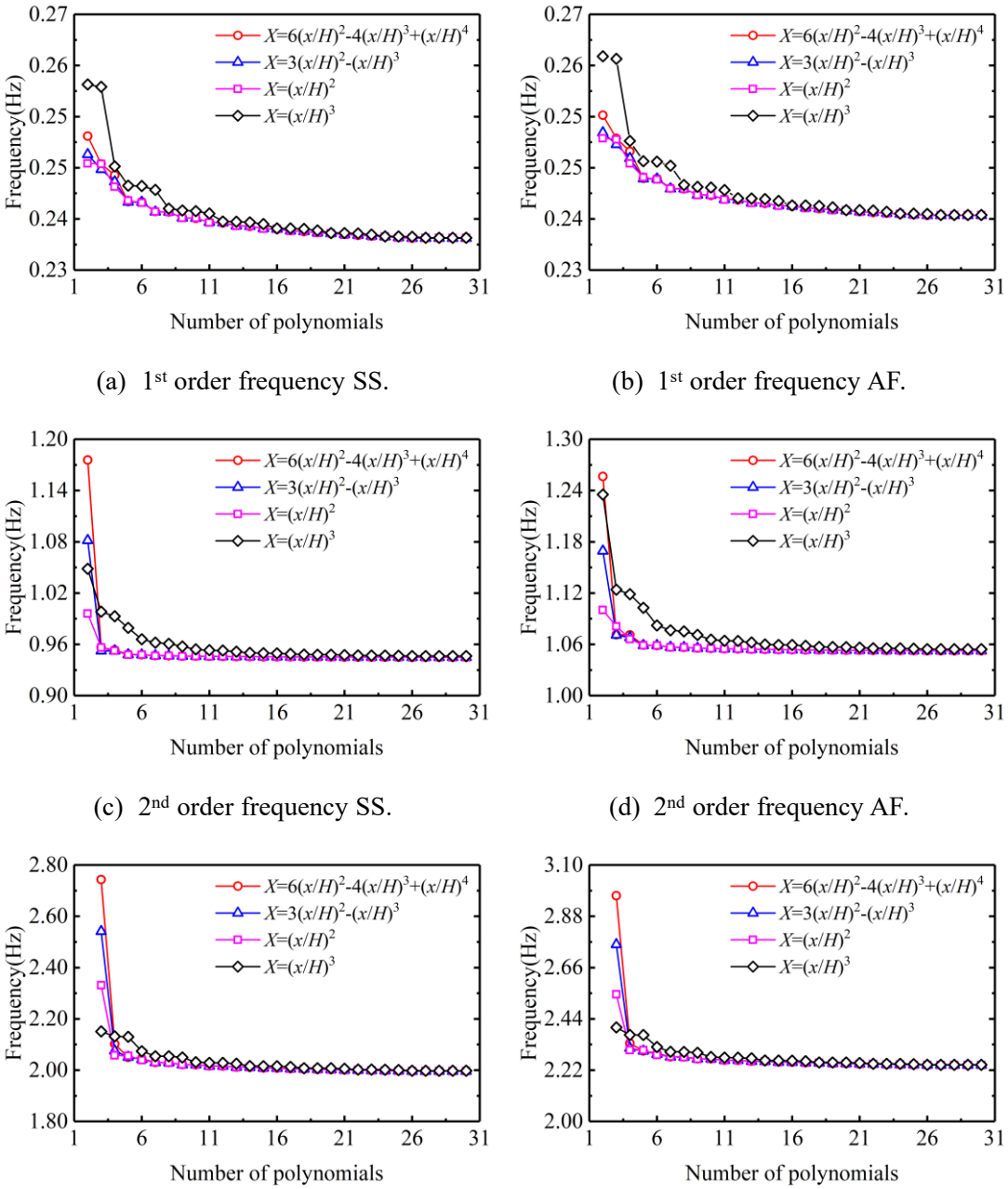

(a) 1st order frequency SS. (b) 1st order frequency AF.

(c) 2nd order frequency SS. (d) 2nd order frequency AF.

(e) 3rd order frequency SS. (f) 3rd order frequency AF.

Fig. 12 Convergence analysis for first three order frequencies.

Table 5 Convergence results obtained from constructing $\phi_0(x)$ with different curves.

Order	Direction	$f_{\text{Eq. (57)}}$/Hz	$f_{\text{Eq. (58)}}$/Hz	$f_{\text{Eq. (59)}}$/Hz	$f_{\text{Eq. (60)}}$/Hz	s/Hz
1st	SS	0.23739	0.23741	0.23743	0.23746	2.6×10^{-5}
	AF	0.24099	0.24101	0.24103	0.24107	3.0×10^{-5}
2nd	SS	0.95463	0.95463	0.95464	0.95607	6.2×10^{-4}
	AF	1.0634	1.0636	1.0634	1.0652	7.5×10^{-4}
3rd	SS	2.0167	2.0168	2.0170	2.0182	6.0×10^{-4}
	AF	2.2648	2.2649	2.2651	2.2660	4.7×10^{-4}

3.4 Validation and comparison

Based on the numerical examples, the SCHTs with pretension force P from 0 to 48 MN are used to analyze the errors of the proposed solution. Table 6 to Table 8 show the comparison between the proposed solution and the numerical solution, where the relative error ξ is defined as

$$\xi = \frac{\left| f_{\text{pro}} - f_{\text{num}} \right|}{f_{\text{pro}}} \times 100\% , \tag{62}$$

where f_{pro} denotes the results of the proposed solution, f_{num} denotes the results of the numerical solution.

Table 6 Comparison of 1st order natural frequency.

P/MN	1st order natural frequency (SS)			1st order natural frequency (AF)		
	f_{pro} (Hz)	f_{num} Hz)	ξ	f_{pro} (Hz)	f_{num} Hz)	ξ
0	0.24036	0.24011	0.104%	0.24415	0.24380	0.143%
8	0.23950	0.23930	0.083%	0.24326	0.24295	0.127%
16	0.23863	0.23847	0.067%	0.24235	0.24209	0.107%
24	0.23774	0.23764	0.042%	0.24142	0.24122	0.083%
32	0.23684	0.23678	0.025%	0.24048	0.24033	0.062%
40	0.23592	0.23591	0.004%	0.23952	0.23942	0.042%
48	0.23498	0.23502	0.017%	0.23854	0.23850	0.017%

Table 7 Comparison of 2nd order natural frequency.

P/MN	1st order natural frequency (SS)			1st order natural frequency (AF)		
	f_{pro} (Hz)	f_{num} Hz)	ξ	f_{pro} (Hz)	f_{num} Hz)	ξ
0	0.95976	0.96165	0.197%	1.0702	1.0707	0.046%
8	0.95733	0.95919	0.194%	1.0673	1.0677	0.037%
16	0.95488	0.95672	0.193%	1.0644	1.0648	0.038%
24	0.95242	0.95423	0.190%	1.0615	1.0618	0.028%
32	0.94994	0.95173	0.188%	1.0585	1.0588	0.028%
40	0.94745	0.94921	0.186%	1.0555	1.0558	0.028%
48	0.94494	0.94668	0.184%	1.0526	1.0527	0.010%

Table 8 Comparison of 3rd order natural frequency.

P/MN	1st order natural frequency (SS)			1st order natural frequency (AF)		
	f_{pro} (Hz)	f_{num} Hz)	ξ	f_{pro} (Hz)	f_{num} Hz)	ξ
0	2.0047	1.9433	3.063%	2.2478	2.1960	2.303%

8	2.0033	1.9420	3.060%	2.2468	2.1950	2.305%
16	2.0019	1.9406	3.062%	2.2458	2.1941	2.302%
24	2.0005	1.9392	3.064%	2.2448	2.1932	2.299%
32	1.9990	1.9378	3.062%	2.2438	2.1923	2.295%
40	1.9976	1.9364	3.064%	2.2428	2.1913	2.296%
48	1.9962	1.9351	3.061%	2.2418	2.1904	2.293%

Overall, the results of the proposed solution agree well with those of the numerical solution. Within the scope of this study, the minimum (maximum) relative errors about the 1st order natural frequency are 0.004% (0.143%), while those about the 2nd and 3rd orders natural frequencies are 0.010% (0.197%) and 2.293% (3.063%), respectively. In addition, the first three orders natural frequencies display different degrees of decrease as the prestress increases. Taking the side-to-side vibration as an example, when the prestressing force P increases from 0 to 48 MN, the first three natural frequencies decrease by 2.24%, 1.54%, and 0.42%, respectively. It indicates that the prestress mainly reduces the lower order natural frequencies, while it has slight influence on the higher order natural frequencies.

4. Analysis and discussion

As mentioned above, the fundamental frequency of the hybrid tower (1st order natural frequency) needs to be kept away from the frequency range formed by f_{1p} and f_{3p} to avoid the resonance response. To study the correlation between the fundamental frequency and the design parameters, a parametric analysis is conducted based on the numerical example depicted in subsection 3.1. The parameters to be studied include the geometric dimensions of the concrete portion (D_{1b}, D_{1t}, t_1) and steel portion (D_{3b}, D_{3t}, t_3), the pretension force (P), and the ratio of steel portion length to concrete portion length ($r_{sc}=h_3/h_1$).

4.1 Parametric analysis

Fig. 13 shows the variation of the fundamental frequency to the ratio of steel portion length to concrete portion length (r_{sc}=h_3/h_1) when the other parameters (D_{1b}, D_{1t}, t_1, D_{3b}, P, D_{3t}, t_3) takes different values. It can be seen that with the increase of r_{sc}, the fundamental frequency increases at first and then decreases. In addition, Fig. 13 also illustrates the variation trends of the fundamental frequency to the other parameters. The fundamental frequency has a positive correlation with the dimensions of the concrete portion (D_{1b}, D_{1t}, t_1) but has a negative correlation with the pretension force P. As for the dimensions of the steel portion (D_{3b}, D_{3t}, t_3), the variation trends are non-monotonic. When the proportion of the steel portion is small, the fundamental frequency shows a negative correlation with D_{3b}, D_{3t}, and t_3, while the correlation gradually turns to be positive as r_{sc} increases.

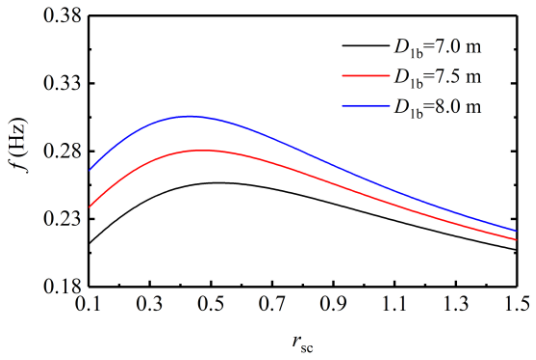

(a) Variation of f to r_{sc} when D_{1b} takes different values.

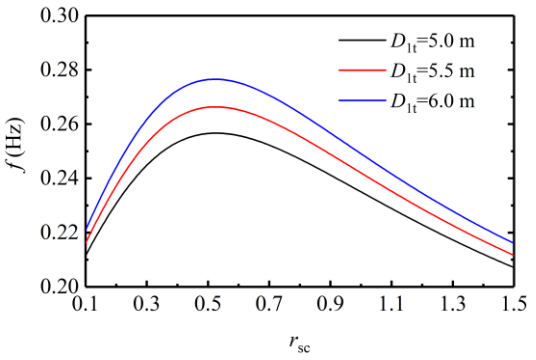

(b) Variation of f to r_{sc} when D_{1t} takes different values.

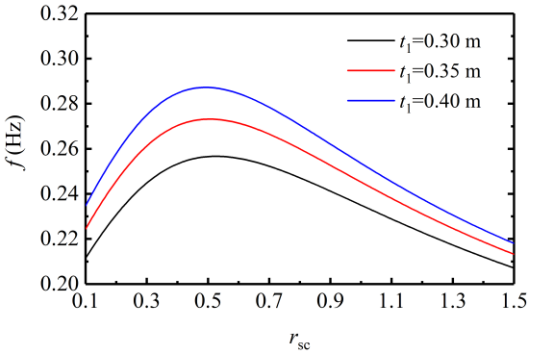

(c) Variation of f to r_{sc} when t_1 takes different values.

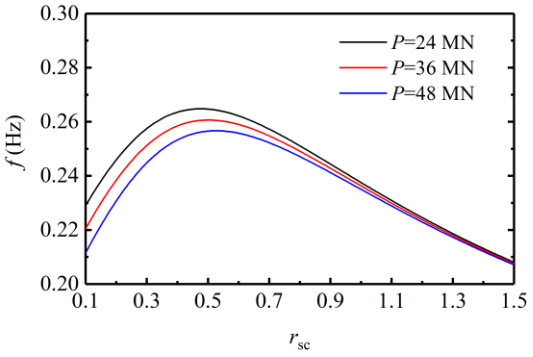

(d) Variation of f to r_{sc} when P takes different values.

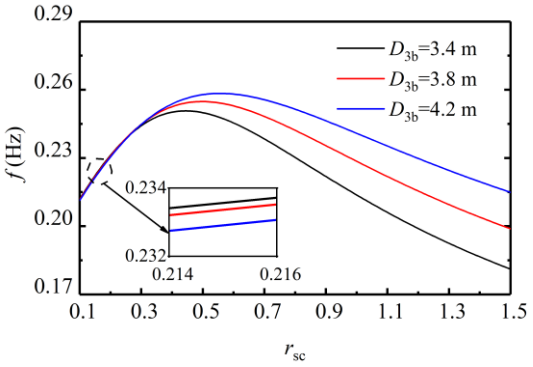

(e) Variation of f to r_{sc} when D_{3b} takes different values.

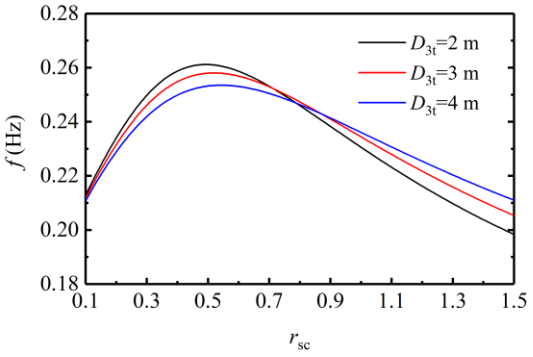

(f) Variation of f to r_{sc} when D_{3t} takes different values.

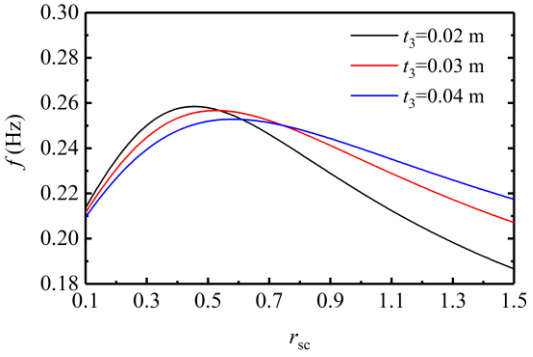

(g) Variation of f to r_{sc} when t_3 takes different values.

Fig. 13 Variation of fundamental frequency to r_{sc}.

To study the sensitivity of the fundamental frequency to the parameters, the differences between curves in the same figure in Fig. 13 are calculated and their

variations with r_{sc} are presented, as shown in Fig 14. It indicates that the sensitivities of the fundamental frequency to the parameters are related to the value of r_{sc}, which are described as follows: 1) With the increase of r_{sc}, the sensitivities of f to D_{1t} and t_1 have a significant tendency to increase and then decrease, while the sensitivity of f to D_{1b} has a slight increase at first and then decreases significantly. 2) The fundamental frequency shows significant sensitivity to the pretension force P when the proportion of the steel portion is small, and the sensitivity decreases drastically as r_{sc} increases. 3) The fundamental frequency shows little sensitivity to D_{3b} when r_{sc} is small, while the sensitivity increases significantly as r_{sc} increases. 4) With the increase of r_{sc}, the sensitivity of the fundamental frequency to the parameters D_{3t} and t_3 shows a trend of increase-decrease-increase. Moreover, there is one intersection between every two curves in Fig. 13 (e)~Fig. 13 (g), corresponding to the zero points in Fig. 14 (e)~Fig. 14 (g). It indicates that for one SCHT with a determined value of r_{sc}, the situation exists where changing the parameters (D_{3b}, D_{3t}, t_3) from one certain value to another certain value does not affect the fundamental frequency of the overall structure.

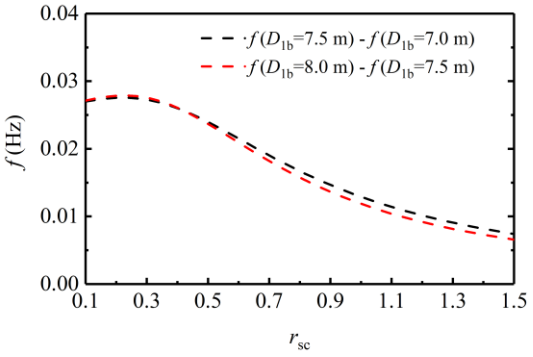

(a) Sensitivity of f to D_{1b} as r_{sc} varies.

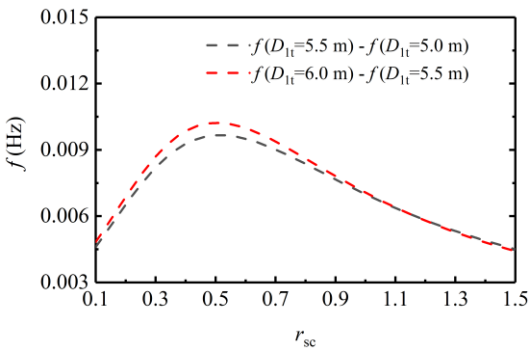

(b) Sensitivity of f to D_{1t} as r_{sc} varies.

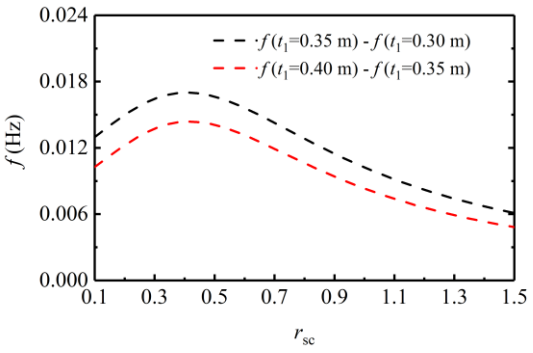

(c) Sensitivity of f to t_1 as r_{sc} varies.

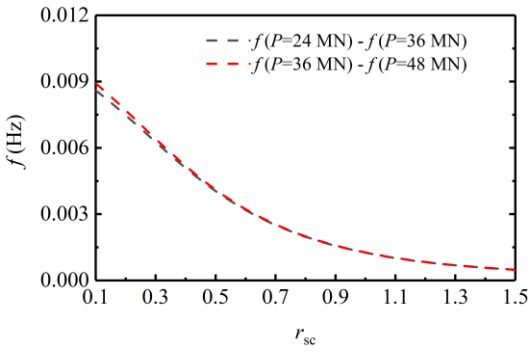

(d) Sensitivity of f to P as r_{sc} varies.

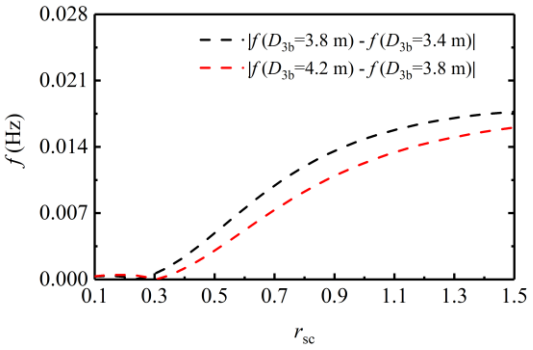

(e) Sensitivity of f to D_{3b} as r_{sc} varies.

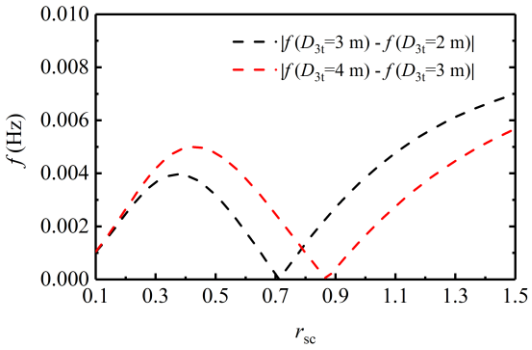

(f) Sensitivity of f to D_{3t} as r_{sc} varies.

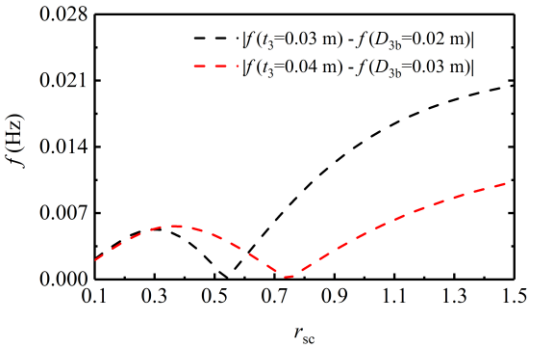

(g) Sensitivity of f to t_1 as r_{sc} varies.

Fig. 14 Sensitivity analysis of fundamental frequency.

4.2 Influence mechanism analysis

In this section, the results of the parametric analysis are explained based on the related formula and theory. According to Eqs. (19) and (32), the increase of pretension force P results in the decrease of total potential energy U but no effect on kinetic energy T. As revealed by Eqs. (47) and (48), when P increases the equivalent section stiffness

$K_{eq}^{(1)}$ decreases, but equivalent mass per unit length $M_{eq}^{(1)}$ remains unchanged. Therefore, the fundamental frequency would decrease with the increase of the pretension force P. Since the pretension force only acts on the concrete portion, thus its effect on the fundamental frequency fades as the proportion of the concrete portion decreases. Therefore, the sensitivity of fundamental frequency to P decreases with the increase of r_{sc}.

According to Eqs. (8)-(13), the section stiffness $K(x)$ is linearly related to the fourth power of the cross-section dimensions (diameters and wall thickness), while the mass per unit length $M(x)$ is linearly related to the second power of the cross-section dimensions. This means that $K(x)$ is more sensitive to the section dimension compared with $M(x)$, that is, the increase of $K(x)$ is greater than that of $M(x)$ when the cross-section dimension increase. In addition, in the formula to compute fundamental frequency Eq. (50), the term representing stiffness is the numerator while the term representing mass per unit length is the denominator. Therefore, in general, the fundamental frequency would increase with the increase of cross-section dimensions. However, besides the influence introduced above, the increase of some cross-section dimensions, especially the parameters of the steel portion, also enlarge the mass of the upper part of the SCHT. As proved in Ref. [20], the increase of mass at the free end of a cantilever beam would reduce the fundamental frequency of the overall structure. Therefore, the correlations between the fundamental frequency and parameters (D_{1b}, D_{1t}, t_1, D_{3b}, D_{3t}, t_3) are affected by those two factors.

The increase of parameter D_{1b} does not affect the upper mass of the concrete

portion, thus increasing fundamental frequency. However, the increase of D_{1t} and t_1 increase the upper mass of the concrete portion, which weakens the positive correlation between the fundamental frequency and parameters D_{1t} and t_1. Besides, the influence of such an effect on the fundamental frequency declines with the increase of r_{sc}, resulting in the sensitivity of fundamental frequency to parameters D_{1t} and t_1 increase at the initial stage. With the continuous increase of r_{sc}, the proportion of the concrete portion decreases, leading to the fading influence of changing parameters of the concrete portion on the fundamental frequency of the overall structure. Therefore, the sensitivity of fundamental frequency to parameters D_{1t} and t_1 presents a variation trend of increase-decrease.

When r_{sc} is small, the proportion of steel portion in the overall SCHT is low, leading to the variation of the parameters of steel portion (D_{3b}, D_{3t}, t_3) causing a slight effect on $M(x)$ and $K(x)$, but affect the mass of upper part of the SCHT apparently. Therefore, the fundamental frequency decreases with the increase of D_{3b}, D_{3t}, and t_3 when r_{sc} is relatively small. However, the parameters of the steel portion (D_{3b}, D_{3t}, t_3) gradually become the leading parameters that affect $M(x)$ and $K(x)$ as r_{sc} increases. This causes the reason for fundamental frequency to increase with D_{3b}, D_{3t}, and t_3 when r_{sc} is relatively large.

It can be seen from Eq. (49) that when the total height of the SCHT H is kept unchanged, the fundamental frequency f is directly related to the equivalent section bending stiffness $K_{eq}^{(1)}$ and the equivalent mass per unit length $M_{eq}^{(1)}$. Therefore, to investigate the influence mechanism of parameters r_{sc} on the fundamental frequency f,

it is necessary to analyze the influence of r_{sc} on parameters $K_{eq}^{(1)}$ and $M_{eq}^{(1)}$. Fig. 15 shows the variations of parameters $K_{eq}^{(1)}/(K_{eq}^{(1)})_{max}$, $M_{eq}^{(1)}/(M_{eq}^{(1)})_{max}$, and $f/(f)_{max}$ with r_{sc}, where $(K_{eq}^{(1)})_{max}$, $(M_{eq}^{(1)})_{max}$, and $(f)_{max}$ respectively denote the maximum value of $K_{eq}^{(1)}$, $M_{eq}^{(1)}$, and f when r_{sc} varies from 0.1 to 1.5. As can be seen from Fig. 15, with the increase of r_{sc}, $K_{eq}^{(1)}$ and $M_{eq}^{(1)}$ present different variation trends. At the initial stage of the increase of r_{sc}, $K_{eq}^{(1)}$ has a slight increase and then decrease while $M_{eq}^{(1)}$ decreases rapidly, resulting in that f increases with r_{sc}. With the continuous increase of r_{sc}, the decreasing rate of $K_{eq}^{(1)}$ almost remains unchanged, while the decreasing rate of $M_{eq}^{(1)}$ gradually declines to such an extent that the variation curve almost becomes a horizontal line, resulting in that f decreases with the increase of r_{sc}.

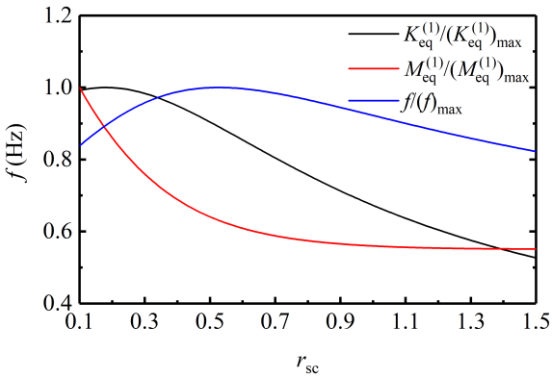

Fig. 15 Variations of $K_{eq}^{(1)}$, $M_{eq}^{(1)}$, and f to r_{sc}.

5. Conclusion

This paper developed a closed-form solution of the fundamental frequency of the steel-concrete hybrid tower (SCHT). In the theoretical derivation, the kinetic energy and potential energy of the SCHT are analyzed, where the abrupt changes of cross-section and material properties, the effect of prestressing, and the mass and rotary inertia of the wind turbine are taken into account. The frequency equation is established based on the law of energy conservation, and a set of orthogonal polynomials generated by

using a Gram-Schmidt process is used to construct the displacement function. Then, based on a numerical example, the convergence of the proposed solution is analyzed, and its effectiveness is validated by comparing the results of the proposed solution with those of the numerical solution (FEM). In addition, by using the proposed solution, a parametric analysis is conducted to investigate the variation rules of the fundamental frequency to the design parameters.

The parametric analysis indicates that the fundamental frequency f increases with the cross-section dimensions of the concrete portion (D_{1b}, D_{1t}, t_1) but decreases with the increase of the pretension force P. The variation rules of the fundamental frequency f to cross-section dimensions of the steel portion (D_{3b}, D_{3t}, t_3) are related to the proportion of steel/concrete portion in the SCHT. When r_{sc} is small, the fundamental frequency f has a negative correlation with the parameters D_{3b}, D_{3t}, and t_3. But this correlation gradually becomes positive with the increase of r_{sc}. Besides, when parameters except r_{sc} remain unchanged, the fundamental frequency f performs a variation trend of initial increase and subsequent decrease with the increase of r_{sc}. In addition, the sensitivity of each parameter to the fundamental frequency f is also related to the value of r_{sc}. With the increase of r_{sc}, the sensitivities of the fundamental frequency f to the cross-section dimensions of the concrete portion (D_{1t}, D_{1b}, t_1) and the steel portion (D_{3t}, D_{3b}, t_3) show tendencies of increase-decrease and increase-decrease-increase, respectively. As for the pretension force P, the tendency performs a continuous decline as the increase of r_{sc}. The influence of prestress on the natural frequency is mainly reflected by Eq. (49), from which it can be seen that the increase of prestress would reduce the equivalent bending

stiffness, thereby causing the decrease of the natural frequency.

Based on the related formula and theory, the phenomena in the parametric analysis are explained, which indicates that the results obtained from the parametric analysis are reasonable. The proposed solution provides an effective approach for determining the fundamental frequency of the SCHT, and the results of the parametric analysis conducted herein may offer guidelines to adjust the parameters in the preliminary design of the SCHT.

Declaration of Competing Interest

The authors declare that they have no known competing financial interests or personal relationships that could have appeared to influence the work reported in this paper.

Acknowledgments

The authors gratefully acknowledge the financial support provided by the Fok Ying Tung Education Foundation (171066) and National Natural Science Foundation of China (51822804).

References

[1] Johansen K. Blowing in the wind: A brief history of wind energy and wind power technologies in Denmark. Energy Policy, 2021;152:112139.

[2] Barra PHA, Carvalho WC, Menezes TS, Fernandes RAS, Coury DV. A review on wind power smoothing using high-power energy storage systems. Renewable and Sustainable Energy Reviews, 2021;137:110455.

[3] Peng XK, Liu ZC, Dong J. A review of multiphase energy conversion in wind power

generation. Renewable and Sustainable Energy Reviews, 2021;147:111172.

[4] Zhang RXX, Shen GQP, Meng N, Wong JKW. An overview on the status quo of onshore and offshore wind power development and wind power enterprise localization in China. International Journal of Green Energy, 2019;16(15):1646-1664.

[5] Dong FG, An XW, Li CY. Performance evaluation of wind power industry chain based on three-stage DEA. Journal of Renewable and Sustainable Energy, 2021;13:033313.

[6] Dai JC, Xin Y, Li W. Development of wind power industry in China: a comprehensive assessment. Renewable and Sustainable Energy Reviews, 2018;97:156-164.

[7] Harrison R, Hau E, Snel H. Large wind turbines design and economics. New York, NY: John Wiley & Sons Ltd, 2000.

[8] McKenna R, vd Leye PO, Fichtner W. Key challenges and prospects for large wind turbines. Renewable & Sustainable Energy Reviews, 2016;53:1212–1221.

[9] NREL, Transportation of Large Wind Components: A Review of Existing Geospatial Data, (Technical Report) National Renewable Energy Laboratory, Golden, CO, USA, 2016.

[10] Way AC, Zijl GPAGV. A study on the design and material costs of tall wind turbine towers in South Africa. Journal of the South African Institution of Civil Engineers, 2015, 57(4):45-54.

[11] Agbayani NA, Vega RE. The rapid evolution of wind turbine tower structural systems: a historical and technical overview. Structures Congress, 2012:1201-1212.

[12] Tricklebank AH, Halberstadt PH. Concrete towers for onshore and offshore wind farms technical report. Camberley: The concrete Center; 2007.

[13] Rebelo C, Moura A, Gerv´asio H, et al. Comparative life cycle assessment of tubular wind towers and foundations–Part 1: structural design. Engineering Structures, 2014;74:283–291.

[14] Deng R, Zhou XH, Deng XW, Ke K, Bai JL, Wang YH. Compressive behaviour of tapered concrete-filled double skin steel tubular stub columns. Journal of Constructional Steel Research, 2021;184:106771.

[15] Vernardos SM, Gantes CJ, Badogiannis EG, Lignos XA. Experimental and numerical investigation of steel-grout-steel sandwich shells for wind turbine towers. Journal of Constructional Steel Research, 2021;184:106815.

[16] Chen JL, Li JW, He XH. Design optimization of steel–concrete hybrid wind turbine tower based on improved genetic algorithm. The structural Design of Tall and Special Buildings, 2020;29(10):1541-7794.

[17] Chen YJ, Zhang YJ, Lin CH, Zhou JK. Optimization and analysis on prestressed concrete-steel hybrid wind turbine tower. Acta Energiae Solaris Sinica, 2021;42(3):121-127 (in Chinese).

[18] Jin QX, Li VC. Development of lightweight engineered cementitious composite for durability enhancement of tall concrete wind towers. Cement and Concrete Composites, 2019;96:87-94.

[19] Jin QX, Li VC. Structural and durability assessment of ECC/concrete dual-layer system for tall wind turbine towers. Engineering Structures, 2019;196:109338.

[20] Clough RW, Penzien J. Dynamics of structures. 2nd Ed. New York: McGraw-Hill; 1993.

[21] Wu QY, Feng H, Xiao SY, Zhu HP, Bai XX. Passive control analysis and design of twin-tower structure with chassis. International Journal of Structural Stability and Dynamics, 2020;20(6):2040010.

[22] Wu JB, Chen B, Song XX. Wind-induced response control of a television transmission tower by piezoelectric semi-active friction dampers. International Journal of Structural Stability and Dynamics, 2022;22(6):2250064.

[23] Harte R, Gideon PAG. Van Z. Structural stability of concrete wind turbines and solar chimney towers exposed to dynamic wind action. Journal of Wind Engineering & Industrial Aerodynamics, 2007;95(9):1079-1096.

[24] Damiani RR. Design of offshore wind turbine towers. Offshore Wind Farms. Woodhead Publishing, 2016:263-357.

[25] Xie F, Aly AM. Structural control and vibration issues in wind turbines: A review. Engineering Structures, 2020;210:110087.

[26] Ghaemmaghami A, Kianoush R, Yuan XX. Numerical modeling of dynamic behavior of annular tuned liquid dampers for applications in wind towers. Computer-Aided Civil and Infrastructure Engineering, 2013;28(1):38–51.

[27] Kenna A, Basu B. A finite element model for pre-stressed or post-tensioned concrete wind turbine towers. Wind Energy, 2015;18(9):1593–610.

[28] Bi JH, Ren HP, Yin YB. Seismic analysis of pre-stressed reinforced concrete wind-turbine tower. Journal of Tianjin University, 2011;44(2):126-133 (in Chinese).

[29] Yue YC, Tian JJ, Mu QY, Chen TB, Peng L, Lu X, Liu J. Feasibility of segmented concrete in wind turbine tower: Numerical studies on its mechanical performance. International Journal of Damage Mechanics, 2021;30(4):518-536.

[30] de Lana JA, Júnior PAAM, Magalhães CA, et al. Behavior study of prestressed concrete wind-turbine tower in circular cross-section. Engineering Structures, 2021;227: 111403.

[31] Vugts JH. Considerations on The Dynamics of Support Structures for An OWEC. Delft University of Technology. Netherlands, 2000.

[32] Tempel JVD. Design of Support Structures for Offshore Wind Turbines. Delft University of Technology, Netherlands, 2006.

[33] Yang CB, Wang R, Zhang JM. A simplified method for analyzing the fundamental frequency of monopile supported offshore wind turbine system design. Earthquake Engineering & Engineering Vibration, 2018;17:893-901.

[34] Gu CJ, Chen DY, Liu FF, Fang K, Guo D, Marzocca P. Dynamic analysis of flexible wind turbine tower by a transfer matrix method. International Journal of Structural Stability and Dynamics, 2021;21(10):2150142.

[35] Liu HB, Wang LL, Tan GJ, Cheng YC, Wu CX. Effect of prestress force on natural frequency of external prestressed simply supported steel beam. Journal of Jilin University (Engineering and Technology Edition), 2013;43:81-85 (in Chinese).

[36] Abraham MA, Stubbs N. Loss of prestress prediction based on nondestructive damage location algorithms. Proceedings of Spie the International Society for Optical Engineering, 1995.

[37] Saiidi M, Douglas B, Feng S. Prestress Force Effect on Vibration Frequency of Concrete Bridges. Journal of Structural Engineering, 1994;120(7):2233-2241.

[38] Huang XG, Li BK, Zhou XH, Wang YH, Zhu RH. Geometric optimisation analysis of Steel–Concrete hybrid wind turbine towers. Structures, 2022;35:1125-1137.

[39] Shu C. Differential Quadrature and Its Application in Engineering. Springer London, 2000.

[40] Wang C, Liu RQ, Huang JP. Geometrically Nonlinear Dynamic Response of Perforated Plates by Modified Differential Quadrature Method. International Journal of Structural Stability and Dynamics, 2021;21(7):2150097.

[41] Bernuzzi C, Crespi P, Montuori R, et al. Resonance of steel wind turbines: problems and solutions. Structures, 2021;32:65–75.

[42] Mama F, Wolfram K. Orthogonal Polynomials. Birkhäuser Cham; 2020.

[43] Bhat RB. Natural frequencies of rectangular-plates using characteristic orthogonal polynomials in Rayleigh-Ritz method. Journal of sound and vibration,1985;102(4):493-499.

[44] Wachirawit S, Nuttawit W, Monsak P. Dynamic Analysis of Functionally Graded SandwichPlates under Multiple Moving Loads by Ritz Method with Gram–Schmidt Polynomials. International Journal of Structural Stability and Dynamics, 2021;21(10):2150138.

[45] Jonkman J, Butterfield S, Musial W, Scott G. Definition of a 5-MW reference wind turbine for offshore system development Technical Report No NREL/TP-500-38060. Golden (CO): National Renewable Energy Laboratory; 2009.

[46] Li P, Wang JL. Comparison of FEM simulation methods of prestressed reinforced concrete members. Journal of Chongqing Jiaotong University (natural science) 2010;29(1):27-29 (in Chinese).

[47] Singiresu SR. The Finite Element Method in Engineering. Butterworth-Heinemann, 2018.

[48] NB/T 10311-2019, Code for design of wind turbine foundations for onshore wind power projects, China Water & Power Press, Beijing, 2019 (in Chinese).